Talanta 233 (2021) 122520

Contents lists available at ScienceDirect

Talanta

journal homepage: www.elsevier.com/locate/talanta

A novel affinity peptide–antibody sandwich electrochemical biosensor for PSA based on the signal amplification of MnO_2-functionalized covalent organic framework

Jing Zheng [a,1], Hui Zhao [b,1], Guobao Ning [a], Weijie Sun [c], Li Wang [a], Huan Liang [a], Hanbin Xu [a], Chaoyong He [b], Hui Zhao [c,*], Can-Peng Li [a,**]

[a] Key Laboratory of Medicinal Chemistry for Natural Resource-Ministry of Education, School of Chemical Science and Technology, Yunnan University, 2 North Cuihu Road, Kunming, 650091, People's Republic of China
[b] Department of Urology, The First Affiliated Hospital of Kunming Medical University, 295 Xichang Road, Kunming, 650032, People's Republic of China
[c] Laboratory for Conservation and Utilization of Bio-resource, Yunnan University, 2 North Cuihu Road, Kunming, 650091, People's Republic of China

ARTICLE INFO

Keywords:
Electrochemical biosensor
Prostate-specific antigen
Affinity peptide
Polydopamine-modified boron-doped carbon nitride
MnO_2 functionalized COF

ABSTRACT

This work describes a novel affinity peptide–antibody sandwich electrochemical strategy for the ultrasensitive detection of prostate-specific antigen (PSA). Herein, polydopamine-coated boron-doped carbon nitride (Au@P-DA@BCN) was synthesized and used as a sensing platform to anchor gold nanoparticles and immobilize primary antibody. Meanwhile, AuPt metallic nanoparticle and manganese dioxide (MnO_2)-functionalized covalent organic frameworks (AuPt@MnO_2@COF) was facilely synthesized to serve as a nanocatalyst and ordered nanopore for the enrichment and amplification of signal molecules (methylene blue, MB). PSA affinity peptide was bound to AuPt@MnO_2@COF to form Pep/MB/AuPt@MnO_2@COF nanocomposites (probe). The peptide–-PSA–antibody sandwich biosensor was constructed, and the redox signal of MB was measured with the existence of PSA. The fabricated sensor exhibited a linear response (0.00005–10 ng mL^{-1}) with a low detection limit of 16.7 fg mL^{-1} under the optimum condition. Additionally, the sensor showed an excellent selectivity, ideal repeatability, and good stability for PSA detection in real samples. Furthermore, the porous structure of COF can enrich more MB molecules and increase the sensitivity of the biosensor. This study provides an efficient and ultrasensitive strategy for PSA detection and broadens the use of organic/inorganic porous nanocomposite in biosensing.

1. Introduction

Prostate cancer (PCa) is a common tumor in men with an incidence rate of 25% among all diagnosed cancers, and its death rate ranks second following lung and bronchus cancer [1]. Prostate-specific antigen (PSA) is an effective marker for PCa diagnose [2]. PSA is also called human glandular kallikrein 3 and a member of the kallikrein family. PSA exists in the serum of patients with PCa and is secreted by prostate epithelial cells [1]. Inactive proPSA is activated to PSA under normal circumstances. Protease inhibitors absorb and inactivate the PSA that enter the circulation via proteolysis and then release free PSA. Proteolysis is inactivated in PCa, and the efficiency of the lysis of proPSA to PSA becomes lower. Therefore, the total PSA concentration in the serum increases [2]. Serum PSA concentration in healthy men is 0–4.0 ng mL^{-1}. Generally, a PSA concentration higher than 4 ng mL^{-1} is considered abnormal [3,4]. Therefore, developing a method to detect PSA accurately is important. Various strategies, including surface-enhanced Raman scattering-based immunoassay [5], fluorescence immunoassay [6], surface plasmon resonance [7], photoelectrochemistry [8], plasmonic enzyme-linked immunosorbent assay [9], and mass spectrometric immunoassay [10], have been applied for PSA detection. However, many of these assays are time consuming, have difficult pretreatment, or require expensive equipment, which limit their application in clinical diagnosis and analysis. Accordingly, developing a

* Corresponding author.
** Corresponding author.
E-mail addresses: zhaohui@ynu.edu.cn (H. Zhao), lcppp1974@sina.com (C.-P. Li).
[1] These authors contributed equally to this work.

https://doi.org/10.1016/j.talanta.2021.122520
Received 9 January 2021; Received in revised form 5 May 2021; Accepted 11 May 2021
Available online 25 May 2021

fast, easy, efficient, and low-cost strategy for PSA detection is urgently needed.

Boron-doped carbon nitride (BCN) is a heteroatom-doped 2D carbon material. Heteroatom-doped carbon materials are one of the most outstanding materials used in gasoline batteries, hydrogen storage, and supercapacitors [11]. Previous studies have shown that 4-pyridylboronic acid can be used to prepare BCN nanomaterials with low toxicity and high stability through a one-step calcination method [12]. However, until now, few applications of BCN nanosheets were reported in electrochemical sensors. Polydopamine (PDA), as a conductive polymer coating material, can be easily deposited on almost all types of inorganic and organic materials and has a controlled film thickness and long-term stability [13]. Recently, Wang et al. reported that PDA coating on can increase the conductivity and stability of multi-walled carbon nanotubes for the detection of carcinoembryonic antigen [14]. Thus, PDA-modified BCN was expected to adhere on the electrode surface stably and play an efficient effect as a substrate material for electrochemical biosensor.

Covalent organic frameworks (COF) are a kind of burgeoning polymers with programmable periodic skeletons and ordered nanopores. COF consists of an accurate organization of organic building units with 2D or 3D porous crystalline structures connected by covalent binding. Recently, COF has been applied in some areas, including energy storage, gas storage or separation, and photocatalysis [15–18]. However, the layers are closely arranged during the synthesis of COF, which hides the active sites, leading to a decrease in the utilization of redox active sites [19]. A previous study has shown a new method to enhance the active sites by dividing the layered COF into several layers of peeled nanosheets. A new 2D COF was synthesized based on Schiff reaction. Manganese dioxide nanoparticles (MnO_2) were introduced onto the material, whose synergistic effect can effectively protect COF from aggregation during use and thus further improve the long-term stability of the composite [19]. A previous study has shown that MnO_2 has excellent catalytic effect on the reduction reaction of methylene blue (MB) [20]. MB is an aromatic heterocyclic dye and a common probe material for electrochemical sensors and biosensors. The pores in COF have benzene ring-containing ligands, which can be combined with MB [3]. Therefore, the integration of COF and MnO_2 may potentially be applied in the amplification of MB signal.

Electrochemical immunosensors are one of the most efficient sensors for the detection of a variety of disease targets through antibody–antigen binding reactions [21]. Immunosensors have two main types: label–free and sandwich-type immunosensors [22]. The traditional sandwich–type immunosensor uses pair antibodies as recognition molecules to specifically bind different epitopes of the same antigen. However, antibodies have high cost, long production cycle time, and difficult screening operation, which makes its application impractical. Compared with antibodies, peptides are easily synthesized in large quantities and can also be chemically modified to change their affinity, stability, and solubility. In particular, peptides can exhibit antibody-like affinity for their receptors [23]. Hence, peptides could be an attractive alternative to antibodies. A previous study showed that PSA affinity peptide (CGGGGMERCPIKMFYNLGSPYMNI) has a dissociation constant (K_d) of 0.8 ± 0.2 nM with PSA and could tightly bind to PSA [24]. However, to the best of our knowledge, no studies have focused on the use of PSA affinity peptide as a specific recognition molecule for the electrochemical detection of PSA. Therefore, in the present work, peptide was used as a replacement of secondary antibody to recognize PSA.

In this study, we first proposed an original strategy for detecting PSA based on affinity peptide–antibody sandwich electrochemical assay using PDA–coated BCN as the substrate platform and MnO_2@-COF–enriched MB as the signal amplification platform and probe material. Furthermore, AuPt metallic nanoparticles (AuPt NPs) in the probe material can play double effects in amplifying electrochemical signals. The biosensor showed lower limit of detection (LOD), excellent specificity, and ideal stability and can be used in PSA detection in diagnosis and analysis of PCa.

2. Materials and methods

2.1. Material, reagents, apparatus, and electrochemical measurements

Material, reagents, apparatus, electrochemical measurements, cell culture and protein extraction were presented in the Supporting Inf**ormation**.

2.2. Preparation of BCN, PDA@BCN, and Au@PDA@BCN

BCN nanosheets were obtained by one-step calcination process based on a previous method [12]. Briefly, 5 g 4-pyridylboronic acid with corundum boat was placed in a pipe furnace and heated to 800 °C in N_2 atmosphere for 3 h to obtain a black powder. Next, PDA@BCN was synthesized by mechanical mixing method [13]. BCN (1 mg) and DA (2 mg) were added into 1 mL of Tris–HCl buffer (100 mM, pH 8.5) and sonicated for 30 min. Afterward, the mixed solution was stirred at room temperature until the solution turned black. The as–prepared PDA@BCN nanocomposite was centrifuged at 10,000 rpm for 15 min and washed three times with deionized water (DW). Finally, PDA@BCN was dispersed in 1 mL of DW for use.

Au@PDA@BCN was prepared by mechanical mixing process. First, Au nanoparticles (Au NPs) were prepared by sodium citrate reduction method. $HAuCl_4$ (500 μL, 23.46 mM) was added to 50 mL of DW and vigorously stirred at 110 °C for 10 min. Then 5 mL of 14.55 mM sodium citrate solution was added into the mixture and refluxed for 30 min until the solution became wine red. The solution was then stirred at room temperature for 15 min to obtain Au NPs. For the preparation of Au@PDA@BCN, 10 mL of the Au NPs solution prepared above was added into 1 mL of PDA@BCN solution and stirred at 4 °C for 4 h. Au@PDA@BCN was gathered via centrifugation at 10,000 rpm for 15 min and washed three times with DW. Finally, the Au@PDA@BCN was dispersed in 1 mL of DW and stored at 4 °C for future use.

2.3. Syntheses of COF, MnO_2@COF, and AuPt@MnO_2@COF

COF was synthesized by a solvothermal method [19]. Typically, 1,2,4,5-Tetrakis-(4-formylphenyl) benzene (TFPB, 25 mg) and 1,4-diaminobenzene (PPDA, 10.8 mg) were added in a 10-mL high–pressure flask and added with 1 mL of mesitylene:dioxane (1:1). The mixture was ultrasonically dispersed at room temperature for 20 min and added with 0.1 mL of 6 M acetic acid. The mixture was passed through three freeze–pump–thaw cycles to degas the reaction mixture and then placed in an oil bath to react at 120 °C for 3 days. After the reaction was completed, the product was cooled and washed three times separately with tetrahydrofuran and acetone. The solid was collected and freeze-dried to obtain pale yellow solid COF. MnO_2@COF was prepared by exfoliating COF according to the strong oxidant embedding process [19]. In a typical process, 20 mg COF and 30 μL of $HClO_4$ aqueous solution (70.0–72.0 wt%) were added into 40 mL of DW and sonicated for 10 min. Then 30 mg of $KMnO_4$ was added into the mixture at 30 °C. The mixture was magnetically stirred for 30 min, sonicated for 2 h. After the reaction was completed, the solution was centrifuged at 8000 rpm for 15 min, and washed thrice with DW. Finally, the composition was freeze–dried to obtain a black powder (MnO_2@COF).

AuPt@MnO_2@COF nanocomposite was synthesized by $NaBH_4$ reduction method [25]. Briefly, 1 mg MnO_2@COF was dispersed in 500 μL of absolute ethanol and sonicated for 1 h to obtain a uniform dispersion. Then, 250 μL of $HAuCl_4$ ethanol solution (1%, w/v) and 250 μL of H_2PtCl_6 ethanol solution (1% w/v) was added to the mixture and sonicated for 1 h. Afterward, 1 mL of 1.2 mM $NaBH_4$ ethanol solution was added under ice bath conditions and sonicated for 1 h. The mixture was centrifuged at 8000 rpm for 15 min, washed three times with DW, and finally resuspended in 500 μL of PBS to obtain 2.0 mg mL^{-1} AuPt@MnO_2@COF dispersion. Finally, the material was stored at 4 °C prior to use.

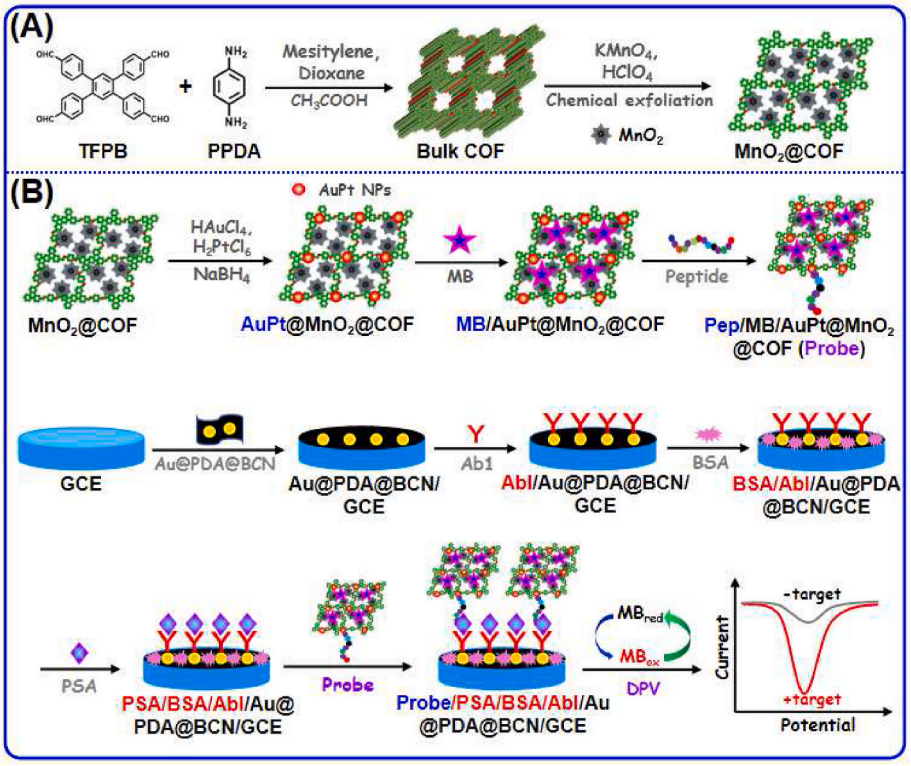

Scheme 1. Synthesis of the MnO_2@COF (**A**) as well as the preparation of Pep/MB/AuPt@MnO_2@COF bioconjuates and the assembly of the biosensor for the PSA (**B**).

2.4. Preparation of Pep/MB/AuPt@MnO_2@COF bioconjugates

Initially, 500 μL of 2.5 mg mL^{-1} MB solution was added to 500 μL of 2.0 mg mL^{-1} AuPt@MnO_2@COF solution and stirred for 12 h. The mixture was then centrifuged at 10,000 rpm for 15 min and washed thrice with DW to remove the free MB. The obtained MB/AuPt@MnO_2@COF nanocomposites were dispersed into 500 μL of PBS. Then, 50 μL of 1.0 mg mL^{-1} PSA affinity peptide was added to the mixture and stirred at 4 °C for 12 h. The mixture was centrifuged at 10,000 rpm for 15 min and washed thrice with PBS to remove unbound peptides. Finally, Pep/MB/AuPt@MnO_2@COF bioconjugates were dispersed in 500 μL of PBS and stored at 4 °C before use.

2.5. Evaluation of catalytic activity of materials

In order to evaluate the catalytic activity of COF, MnO_2@COF, and AuPt@MnO_2@COF, composites for MB reduction, UV–vis spectroscopy of the MB after reduction in the presence of material was monitored. Firstly, 2 mL of 50 mM MB and 0.5 mL of 0.1 M $NaBH_4$ aqueous solutions were mixed in a quartz cuvette, and then 320 μg mL^{-1} of different material was added into the mixed solution, and the time–dependent UV–vis absorption spectra were recorded in the range of 400–800 nm.

2.6. Construction of the modified electrodes

Glassy carbon electrodes (GCEs) were polished with Al_2O_3 powder (0.3 and 0.05 μm), then ultrasonicated with DW for 10 min to remove the surface material, and dried for use. Then, 10 μL of 1 mg Au@PDA@BCN solution was dropped on the electrode surface and dried. The Au@PDA@BCN-modified electrode was incubated overnight in 10 μg mL^{-1} primary antibody (Ab1) at 4 °C. The free Ab1 was washed away with PBS. The Ab1/Au@PDA@BCN–modified GCE was dried, incubated in 2.5 mg mL^{-1} bovine serum albumin (BSA) solution for 40 min to block nonspecific sites, then washed, and dried. Next, 10 μL of different concentrations of PSA were then loaded on the electrode surface, incubated for 1 h, washed, and dried. Finally, the PSA/BSA/Ab1/Au@PDA@BCN–modified electrode was incubated in Pep/MB/AuPt@MnO_2@COF bioconjugates for 1 h and then washed and dried. Scheme 1 illustrates the synthesis process of the MnO_2@COF nanohybrids and the construction of the biosensor.

3. Results and discussion

3.1. Characterization of BCN, PDA@BCN, and Au@PDA@BCN composites

Raman spectroscopy was used to characterize BCN and PDA@BCN. As shown in Fig. 1A, BCN and PDA@BCN showed two characteristic peaks, which correspond to the defect–inducing band at 1325 cm^{-1} and the graphite band at 1572 cm^{-1}. The peaks of PDA@BCN were blue–shifted by 12.44 and 4.65 cm^{-1}, respectively, compared with those in BCN. This result demonstrates that the PDA@BCN was successfully composited. The morphologies of BCN and PDA@BCN were observed by transmission electron microscopy (TEM) and scanning electron microscopy (SEM). The TEM and SEM images of BCN showed a layered and stacked nanosheet structure (Fig. 1C and E). However, the SEM image of PDA@BCN showed that the surface of the BCN nanosheets changed from smooth to rough after PDA was loaded with BCN (Fig. 1F). This change in morphology proved that the PDA was successfully coated with BCN. The X-ray diffraction (XRD) pattern of BCN is shown in Fig. S1A. The two characteristic peaks at 12.62° and 23.94° are ascribed to the graphene-like structure of BCN. This result was consistent with that in a previous literature [26]. As shown in the zeta potential diagrams of BCN, PDA@BCN, and Au@PDA@BCN (Fig. S1C–E), the zeta potential of BCN, which was 4.35 mV, became 0.87 mV when PDA was loaded on BCN because of the negative charge of PDA and became −6.89 mV after loading Au NPs because of the negative charge of Au NPs. The X-ray photoelectron spectroscopy (XPS) images of Au@PDA@BCN

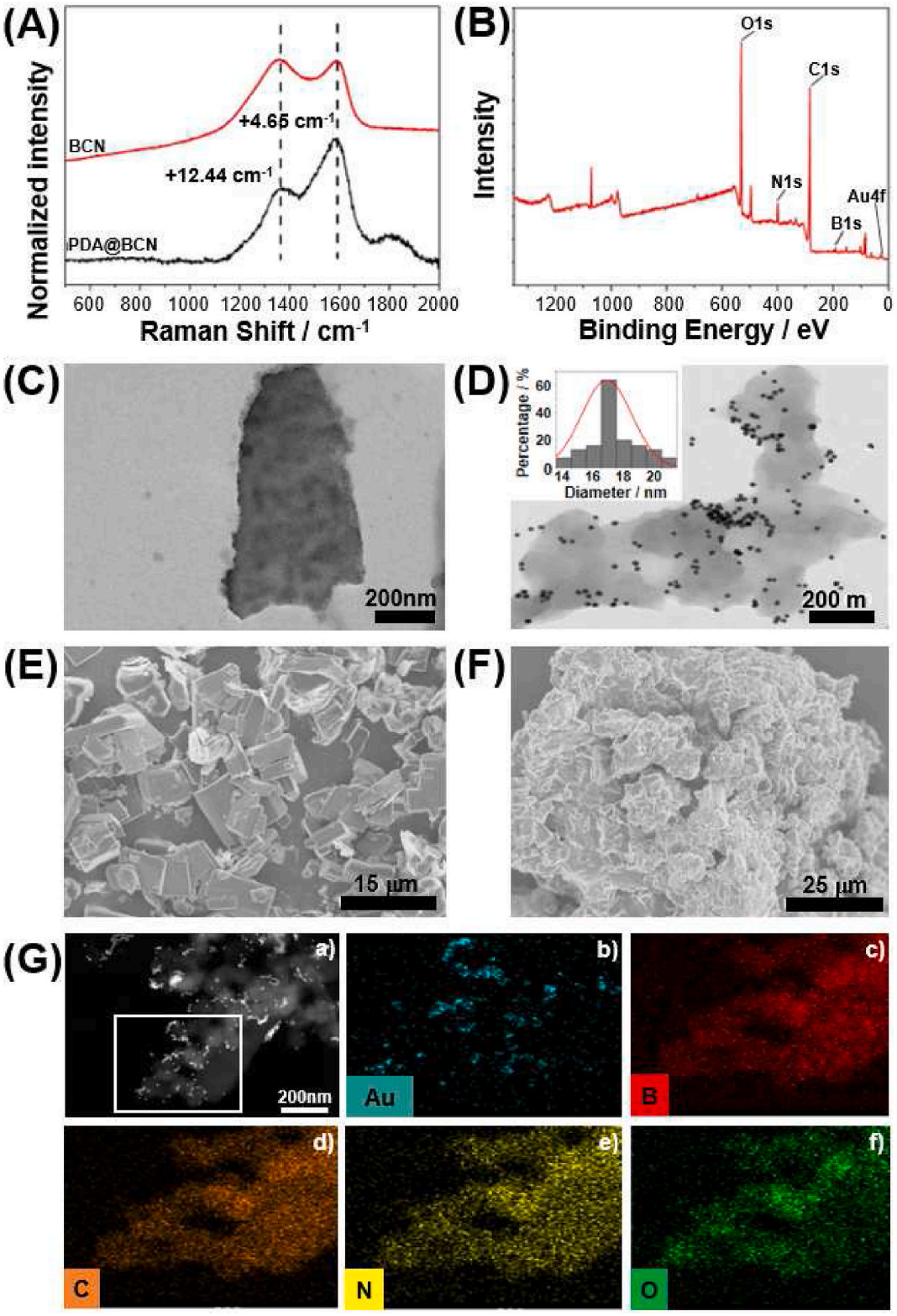

Fig. 1. Characterization of BCN, PDA@BCN, and Au@PDA@BCN. Raman spectra of BCN and PDA@BCN (**A**); XPS Image of Au@PDA@BCN (**B**); TEM images of BCN and Au@PDA@BCN (**C, D**); SEM images of BCN and PDA@BCN (**E, F**); Elemental mapping of Au@PDA@BCN (**G**). a): TEM of Au@PDA@BCN, b): Au, c): B, d): C, e): N, f): O.

nanocomposite show the presence of B and Au elements (Fig. 1B). Similar results were obtained from energy-dispersive X-ray spectroscopy (EDX) analysis, but the peak of B element was not observed because B and C are adjacent elements (Fig. S1B). Element mapping analysis showed that Au, B, C, N, and O elements coexisted (Fig. 1G, a–f). The morphological characteristics of Au@PDA@BCN were also studied by TEM. Fig. 1D shows that Au NPs uniformly adhered on the surface of PDA@BCN, whose average particle size was approximately 17 nm. All the results proved the successful preparation of Au@PDA@BCN.

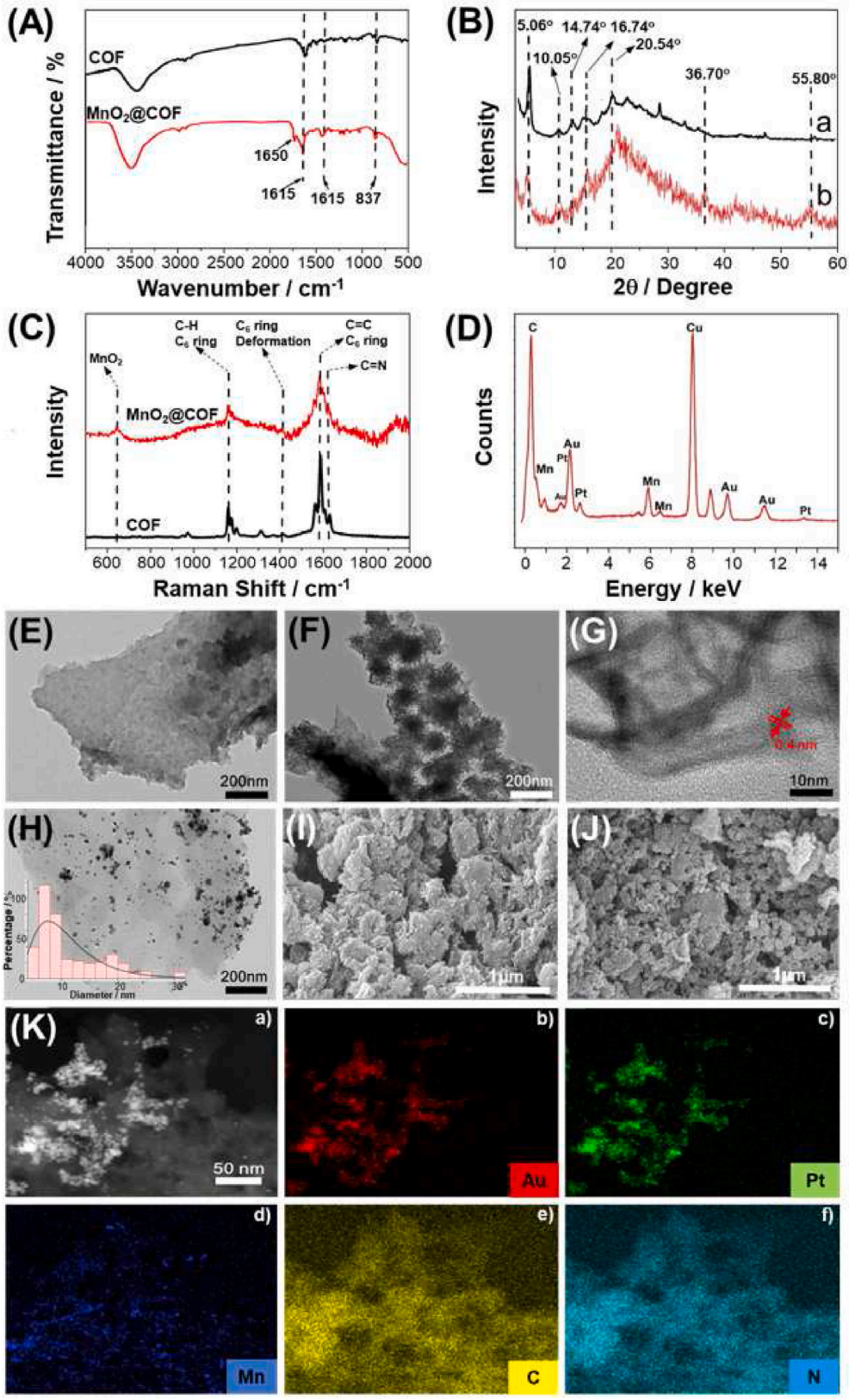

Fig. 2. Characterization of COF, MnO_2@COF, and AuPt@MnO_2@COF. FTIR spectra of COF and MnO_2@COF (**A**); XRD survey spectra of COF and MnO_2@COF (**B**). a, COF; b, MnO_2@COF; Raman spectra of COF and MnO_2@COF (**C**); EDX profiles of AuPt@MnO_2@COF (**D**); TEM images of COF, MnO_2@COF, and AuPt@MnO_2@COF (**E-H**); SEM images of COF and MnO_2@COF (**I, J**); Elemental mapping of Au@MnO_2@COF (**K**). a): TEM of AuPt@MnO_2@COF, b): Au, c): Pt, d): Mn, e): C, f): N. Scale bar of 0.4 nm in Fig. 2G shown the lattice fringe pitch of the (001) plane of MnO_2.

3.2. Characterization of COF, MnO_2@COF, and AuPt@MnO_2@COF composites

The Fourier-transform infrared spectra of COF and MnO_2@COF are shown in Fig. 2A. The peak at 1615 cm^{-1} was due to the C═N group from the reaction product of the aldehyde group and the amino group from TFPB and PPDA, respectively. The peaks at 1500 and 837 cm^{-1} were because of the tensile/bending vibration of the aromatic ring and the aromatic C–H out–of–plane vibration, which demonstrate the successful formation of COF. A new peak around 1650 cm^{-1} was observed

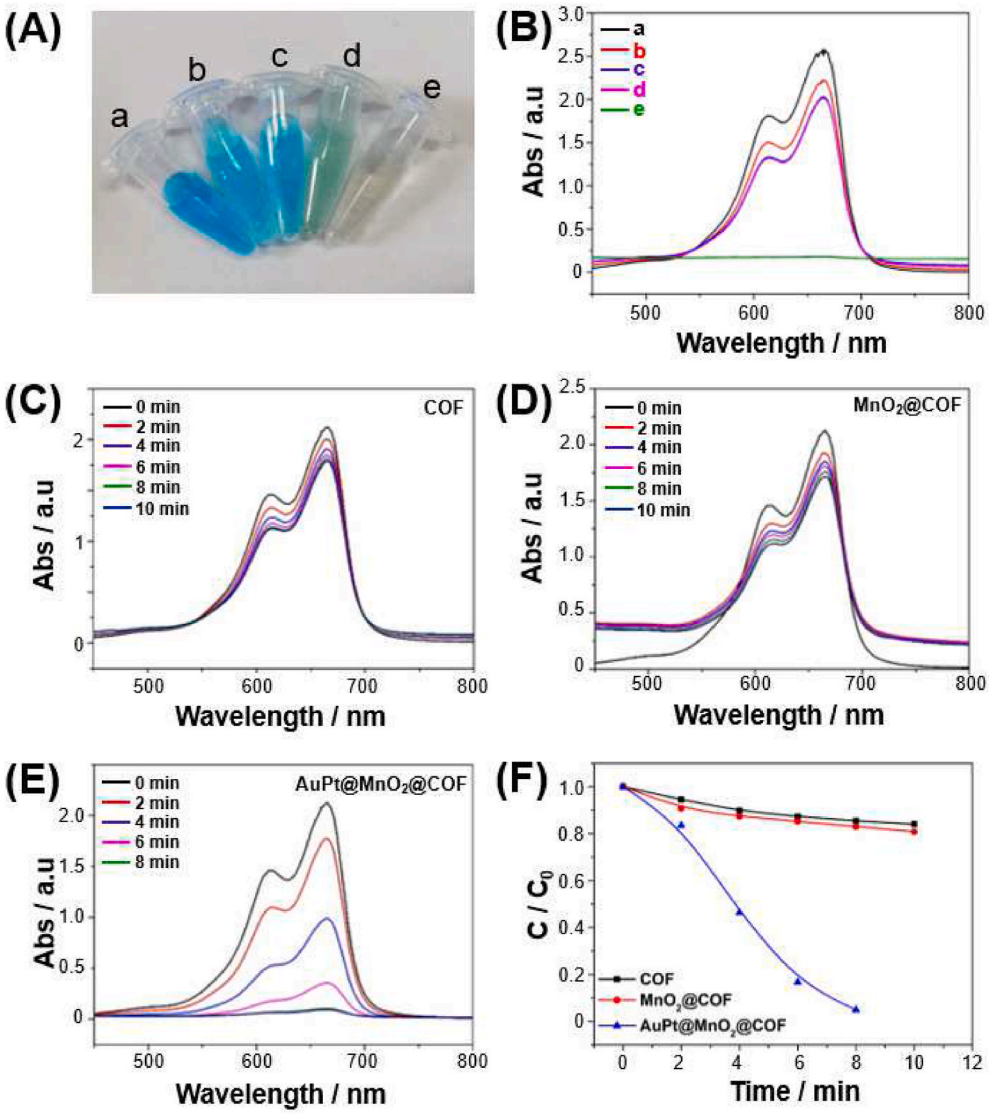

Fig. 3. The color change of the MB solution catalyzed by different nanocatalyst (**A**). a): MB, b): MB + $NaBH_4$, c): MB + $NaBH_4$+COF, d): MB + $NaBH_4$+MnO_2@-COF, e): MB + $NaBH_4$+AuPt@MnO_2@COF; UV–vis absorption spectra of MB solution catalyzed by different materials (**B**); Time-dependent UV–vis absorption spectra for catalytic reduction of MB in the presence of COF (**C**), MnO_2@COF (**D**) and AuPt@ MnO_2@COF (**E**) catalysts; plots of C/C_0 as function of the reaction time for reduction of MB (**F**). (For interpretation of the references to color in this figure legend, the reader is referred to the Web version of this article.)

and indicates that the C═N bond in COF was partially oxidized [19]. The crystal structures of COF and MnO_2@COF were analyzed by XRD measurement. The strong peaks found at 5.06°, 10.5°, 14.74°, 16.74°, and 20.54° in Fig. 2B are assigned to the (110), (220), (510), (330), and (001) crystal planes of COF, respectively [19]. The XRD pattern of MnO_2@COF after loading MnO_2 slightly shifted in the strong diffraction peaks at 5.06° and showed good diffraction peaks for α-MnO_2 at 36.70° and 55.80°. This finding suggests the successful preparation of MnO_2@COF [19,27]. In addition, Raman spectroscopy characterization of COF and MnO_2@COF was performed. The bands at 1633, 1587, 1200, and 659 cm^{-1} in Fig. 2C, belong to the C═N group, the C═C group of the C_6 ring, the deformation vibration of the C in the C_6 ring, the C–H group of the C_6 ring, and the Mn–O stretching vibration, respectively. The peak at 1318 cm^{-1} represents the characteristics of disordered carbon or defective graphite structure. The results are consistent with those in a previous study [19].

Zeta potential characterization was performed to study the charge of the composites. The zeta potential of COF was −13.2 mV, and the zeta potential of MnO_2@COF was −16.7 mV. This difference suggests that MnO_2 was successfully loaded on the surface of COF. The negative potential of the material increased to −19.3 mV after loading AuPt NPs because of its negative charge (Figs. S2D–F). The EDX results showed the coexistence of Au, Pt, C, N, O, and Mn elements in AuPt@MnO_2@COF nanocomposites (Fig. 2D), which indicated the successful preparation of AuPt@MnO_2@COF nanocomposites. Furthermore, XPS was used to determine the composition of AuPt@MnO_2@COF (Fig. S2C). The investigation of the spectrogram proved the existence of Au, Pt, C, N, O, and Mn in the AuPt@MnO_2@COF nanocomposite, and this result was consistent with the EDX results. The SEM, TEM, and element mapping analyses of various materials were performed to better understand the morphology and structure of the composite materials. TEM and SEM images showed that the COF was a multilayer stack structure (Fig. 2E, I). This finding is consistent with that in a previous literature [19]. Layers of the thin film structure of COF were observed and many flower-like MnO_2 particles adhered on the surface of COF after loading MnO_2. These structures can prevent the multilayer nanosheets from falling off during accumulation (Fig. 2F, J). In addition, the detectable lattice fringe pitch of 0.4 nm can be attributed to the (001) plane of MnO_2 (Fig. 2G) [19]. The small nanoparticles observed after loading AuPt NPs indicate that AuPt NPs were anchored on the surface of MnO_2@COF (Fig. 2H). Elemental mapping analysis showed that Au, Pt, Mn, C, and N elements were uniformly dispersed on the surface of AuPt@MnO_2@COF (Fig. 2K, a–f). The results indicated that the AuPt@MnO_2@COF nanocomposite was successfully prepared.

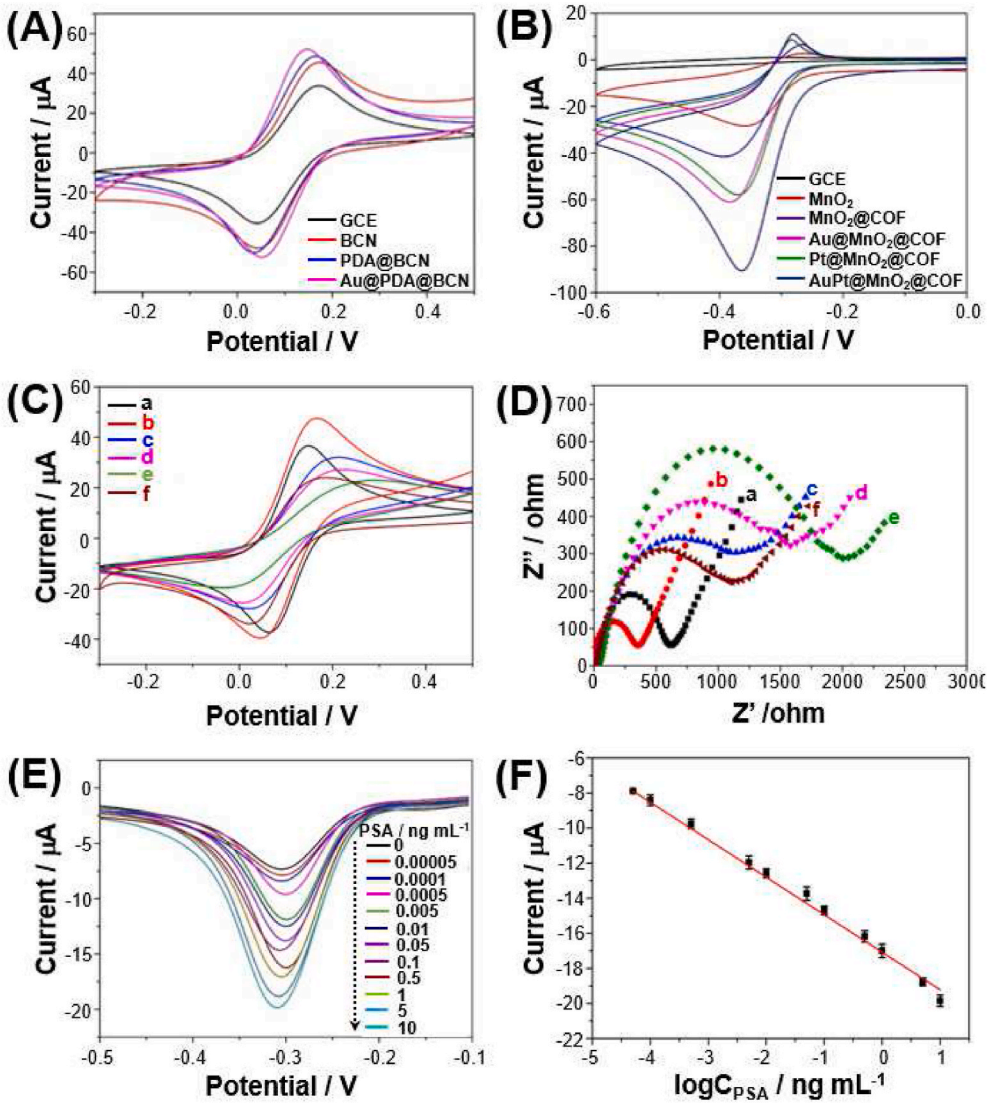

Fig. 4. CV measurements with different materials in 0.1 M PBS containing 2.0 mM $[Fe(CN)_6]^{3-/4-}$ and 0.1 M KCl (**A**); CV measurements of MB on the different electrodes modified with different materials (**B**); Assembly of modified electrodes characterized by CV (**C**) and EIS (**D**) in 0.1 M PBS containing 2.0 mM $[Fe(CN)_6]^{3-/4-}$ and 0.1 M KCl: a, GCE; b, Au@PDA@BCN/GCE; c, Ab1/Au@PDA@BCN/GCE; d, BSA/Ab1/Au@PDA@BCN/GCE; e, PSA/BSA/Ab1/Au@PDA@BCN/GCE; f, Pep/MB/AuPt@MnO_2@COF/PSA/BSA/Ab1/Au@PDA@BCN/GCE; DPV curves for different concentrations of PSA in 0.1 M PBS (**E**); Calibration plot for log [C_{PSA} ng mL^{-1}] *vs.* DPV response in the range of 0.00005–10 ng mL^{-1}. Error bar = standard deviation (SD), (n = 3) (**F**).

3.3. Catalytic activity of COF, MnO_2@COF, and AuPt@MnO_2@COF composites towards MB reduction

The catalytic activity of different materials was investigated by reducing MB from oxidized form (blue) to reduced form (colorless) in the presence of $NaBH_4$. As shown in Fig. 3B, MB showed two characteristic peaks at 664 nm and 613 nm, which are attributed to the monomer and dimer of oxidized MB, respectively [28]. When $NaBH_4$ or $NaBH_4$ and COF was added to the MB solution, the characteristic peaks decreased slightly and the color of MB did not change significantly (Fig. 3A, b, c), suggested that COF had little catalytic effect on the reduction of MB. After MnO_2@COF was added to the mixed solution, the absorbance of the MB decreased and the solution became wathet blue (Fig. 3A, d), indicating that MB was partly reduced by $NaBH_4$ under the catalysis of MnO_2. However, after addition of AuPt@MnO_2@COF, the peak of oxidized MB disappeared entirely and the color of MB solution was colorless (Fig. 3A, e). This result indicated that the AuPt@MnO_2@COF nanocomposite had the more excellent catalytic activity than COF or MnO_2@COF for reduction of MB. The superior catalytic activity for MB reduction may be due to the fine AuPt bimetallic nanoparticles, which were uniformly anchored with MnO_2@COF and played a synergetic catalytic role [29] (Fig. 2K, b, c). Therefore, the AuPt@MnO_2@COF was expected to be used as an excellent nanocomposite for the signal amplification of the electrochemical biosensor in the following experiments.

3.4. Different signal amplification strategies

Excellent electrochemical performance is an important indicator for the construction of an immunosensor. The signal amplification capacity of materials were evaluated by cyclic voltammetry (CV). First, the signal amplification capacity of GCE, BCN, PDA@BCN, and Au@PDA@BCN were measured in 2 mM $[Fe(CN)_6]^{3-/4-}$ and 0.1 M KCl. Fig. 4A shows a pair of typical invertible redox peaks of ferricyanide ions on the GCE. The current response increased markedly when BCN was dropped on the GCE. This finding suggested that BCN can accelerate the electron transfer between the solution and GCE [12]. The current response further increased after PDA@BCN was fixed on the electrode surface because of the excellent electrochemical performance of PDA. The current further increased after Au NPs were anchored on the surface of PDA@BCN probably because of the excellent conductivity of Au NPs. Hence, Au@PDA@BCN was used as a substrate material of GCE. The electrocatalytic performances of GCE, MnO_2, MnO_2@COF, Au@MnO_2@COF, Pt@MnO_2@COF, and AuPt@MnO_2@COF for MB were studied. As shown in Fig. 4B, the modified electrodes have a pair of redox peaks around −0.3 V. GCE showed a smaller current response at approximately −1.80 μA. Compared with GCE, the current response increased to −28.38 μA after MnO_2 was dropped on the electrode

surface because of the catalytic performance of MnO_2 for reduction reaction of MB [30]. The current response further increased to −41.55 μA when MnO_2@COF was fixed on the surface of GCE. This increase was due to the dual effects of prominent enrichment ability of COF and the excellent catalytic ability of MnO_2. The current response increased again after Au NPs or Pt NPs were loaded on the surface of MnO_2@COF. However, the current response was much higher than those of Au- or Pt@MnO_2@COF when AuPt@MnO_2@COF was dropped on the electrode surface. This result suggested that bimetallic AuPt NPs play a crucial role in the catalysis of MB reduction, and therefore effectively amplified the electrochemical signal of MB [25,31]. Interestingly, the electrodes modified by these materials caused little change in the oxidation peak of MB, but their electrochemical signal amplification effect on the reduction peak was obvious because of the irreversible reduction reaction of MB. Thus, AuPt@MnO_2@COF was expected to be used as an outstanding nanocomposite for electrochemical signal amplification in the next experiments.

3.5. Construction of the biosensor

The electrodes modified with different materials were characterized by CV and electrochemical impedance spectroscopy (EIS) to investigate the assembly of nanocomposites on GCE. As shown in Fig. 4C, the current response of Au@PDA@BCN-modified GCE remarkably increased compared with that of GCE alone, because Au@PDA@BCN accelerated the charge transfer and enhanced the conductivity. The decrease in current response when Ab1 was immobilized on the Au@PDA@BCN-modified electrode suggests that Ab1 was successfully loaded on the surface of Au@PDA@BCN. The electrode current further decreased after incubation with BSA, indicating that non-specific sites were successfully blocked. The current peak further decreased to the lowest value when PSA was fixed on the BSA/Ab1/Au@PDA@BCN-modified electrode. This finding indicated that PSA successfully adhered to the modified electrode. However, the peak current increased after incubation with the Pep/MB/AuPt@MnO_2@COF bioconjugate because of the high conductivity of AuPt NPs and the outstanding electrocatalytic capability of MnO_2@COF in the bioconjugates. Moreover, EIS was used to investigate the electron transfer capabilities of the electrodes. As shown in Fig. 4D, the substantial reduction in charge transfer resistance (R_{ct}) after Au@PDA@BCN was modified on GCE proved that Au@PDA@BCN has an excellent conductivity. The increase in R_{ct} after incubation with Ab1 suggested that Ab1 was successfully fixed. The R_{ct} of BSA/Ab1/Au@PDA@BCN-modified GCE further increased after blocking non-specific sites with BSA. The R_{ct} of the modified electrode increased remarkably and reached the maximum when incubated with PSA. Finally, R_{ct} decreased obviously after binding to the Pep/MB/AuPt@MnO_2@COF bioconjugate. This result indicated that the peptide bioconjugates were successfully combined with the modified electrode. These results coincided well with the obtained CV results and confirmed the successful construction of the electrochemical biosensor.

3.6. Experimental optimization conditions

The pH of the detection environment, the incubation time of Pep/MB/AuPt@MnO_2@COF bioconjugates, and the concentration of MnO_2@COF were optimized to investigate the optimum experimental conditions. The current responses were evaluated at the pH of 5.0–8.0. As shown in Figs. S3A and B, the current response reached the maximum at pH 7.0. Hence, pH 7.0 was chosen as the optimal detection condition for the subsequent experiment. In addition, the incubation time of Pep/MB/AuPt@MnO_2@COF bioconjugates with the electrode and the concentration of MnO_2@COF were investigated. The optimal incubation time of Pep/MB/AuPt@MnO_2@COF was 60 min (Fig. S3C), and the optimal concentration of MnO_2@COF was 2.0 mg mL^{-1} (Fig. S3D). Accordingly, these conditions were used in the subsequent experiment.

Table 1
Comparison of various electrochemical immunosensors for PSA.

Electrode	Method	Linear range ($ng{\cdot}mL^{-1}$)	LOD ($pg{\cdot}mL^{-1}$)	Reference
Au/Pd@SnO_2/Au@CMK-3/GCE	DPV	0.01–100	3	[2]
Au@Pene/Au@Fe_3O_4@COF/GCE	DPV	0.0001–10	0.03	[3]
Cu_2O@CeO_2–Au/GCE	i-t	0.0001–100	0.03	[32]
AuPd@Au NCs/GCE	DPV	0.1–50	78	[33]
Au@MnO_2/GOx@CNSs/PWE	DPV	0.005–100	1.2	[34]
Ag NPs@MSNs/GCE	CV	0.05–50	15	[35]
Au-GR/GCE	CV	0–10	590	[22]
Au@Th@GO/PtCu@rGO@g-C_3N_4/GCE	i-t	0.00005–40	0.017	[36]
AuPtAg ANCs/GCE	DPV	0.05–50	17	[37]
Au NPs/CHI/SPE	SWV	1–18	1	[38]
Au NPs/Pd@Nh2-ZIF-67/GCE	i-t	0.0001–50	0.03	[39]
Au@MWCNT@Au NPS/HRPs/AuE	SWV	0.001–30	0.3	[40]
PtCu NHFs/GCE	DPV	0.01–100	3	[41]
Au NPs/magnetic bead-HRP/GCE	i-t	0.5–10	17	[42]
Au@SiO_2/AuE	DPV	1–60000	300	[43]
GQDs-Au NRs/SPE	DPV	0–11.6	140	[44]
Microfluidic immunoarrays	i-t	2.72×10^{-6}-0.712	0.0003	[45]
3D-Printed immunoarrays	ECL	0.0005–10	0.3	[46]
Automated multiplexed ECL immunoarrays	ECL	10×10^{-6}-100×10^{-6}	10×10^{-6}	[47]
MWCNTs-PAMAM/DSP@Au@SiO_2/GCE	LSV	0.001–30	0.7	[48]
Anti-PSA/SP-rGO/GCE	DPV	0.1–5.0 5.0–80	53	[49]
Au@PDA@BCN/AuPt@MnO_2@COF/GCE	DPV	0.00005–10	0.0167	This work

3.7. Detection of PSA by the constructed biosensor

PSA was detected by the constructed biosensor under the optimal detection conditions. Fig. 4E shows the differential pulse voltammetry (DPV) response of the biosensor at different PSA concentrations. The reduction peaks of MB increased proportionally with the concentrations of PSA from 0.00005 ng mL^{-1} to 10 ng mL^{-1}. Fig. 4F shows that the linear relationship between the peak current and the logarithmic concentration of PSA is I (μA) = −2.137 $logC_{PSA}$ ($ng{\cdot}mL^{-1}$) – 17.078 (R^2 = 0.996) with a LOD of 16.7 fg mL^{-1} (S/N = 3). The biosensor had outstanding LOD compared with the previously reported immunosensors (Table 1).

In our work, the satisfactory sensitivity of the constructed biosensor can be ascribed as follows. First, the high stability, good conductivity, and good biocompatibility of BCN and PDA. Second, the rigid pore structure and high specific surface area of COF, which enriched more signal molecules. Meanwhile, COF is a benzene-riched pored material and can form a “host-guest” complex with MB through non-covalent interactions, such as π−π, hydrophobic, and electrostatic interactions. The benzene-riched pore may enhance electron transfer of the signal molecule (MB) and amplify the electrochemical signal. We have showed an efficient method for signal amplification of the biosensor based on the enrichment of signal molecule of COF [4]. In the present study, the strategy of signal amplification was designed by introducing not only COF but also bimetallic nanoparticles and MnO_2, which was expected to play multi-roles in signal amplification based on the excellent enrichment of MB by COF and further being catalyzed by AuPt and MnO_2. Therefore, the excellent catalytic activity of AuPt@MnO_2@COF may result in the efficient amplification of electrochemical signal of

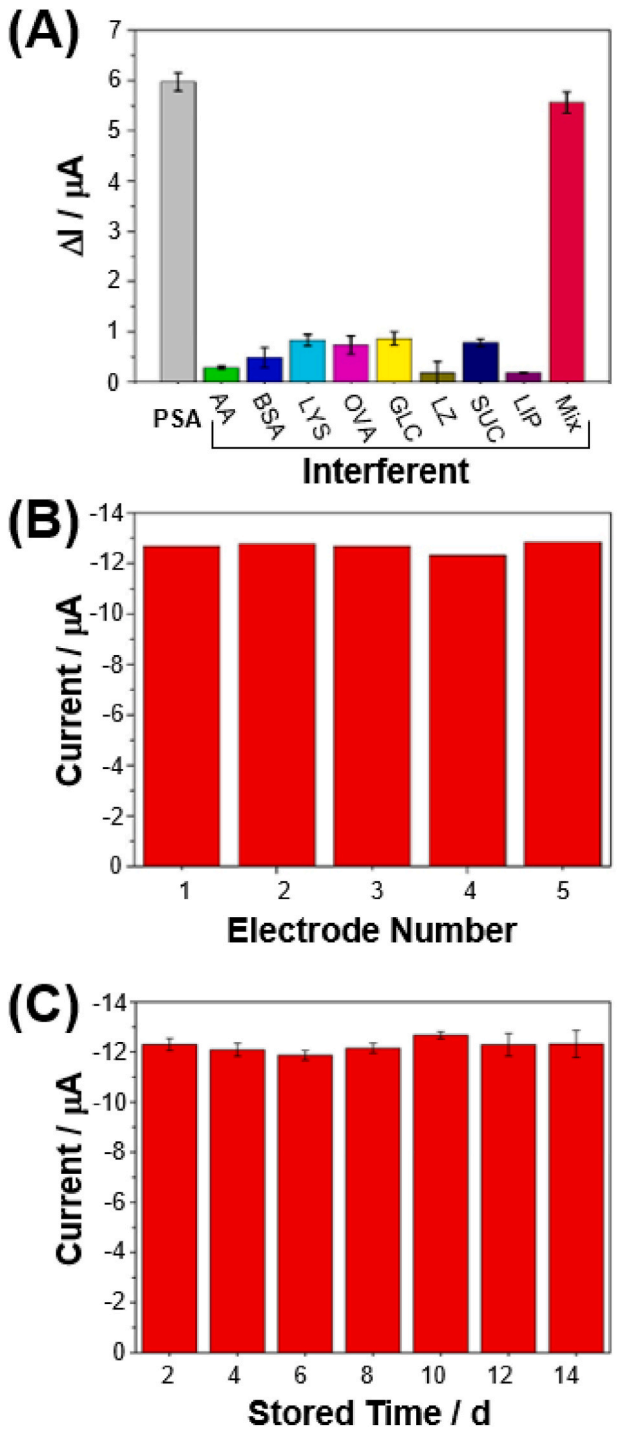

Fig. 5. Selectivity (**A**), repeatability (**B**), and stability (**C**) of the biosensor. Interferents: AA, ascorbic acid; BSA, bovine serum albumin; LYS, lysine; OVA, ovalbumin; GLC, glucose; LZ, Lysozyme; SUC, source; LIP, lipase. Interferent concentration: 100 ng mL^{-1}.

biosensor.

For the specific recognition molecule for PSA, in the present study, an affinity peptide instead of an antibody was used in the construction of the biosensor. It is worthy to note that the peptide has the smaller molecular weight than antibodies and can recognize more target molecules and thus resulting in higher sensitivity. From the economic viewpoint, the cost of product of peptide is much lower than the antibody and therefore the cheap manufacture of biosensor can be expected.

Table 2
Determination of PSA in artificial serum samples using ELISA and constructed electrochemical sensor (n = 3).

Sample	Added ($ng{\cdot}mL^{-1}$)	Founded[a] ($ng{\cdot}mL^{-1}$)	Founded[b] ($ng{\cdot}mL^{-1}$)	RSD[b] (%)	Recovery[b] (%)
1	0.1	0.11 ± 0.015	0.10 ± 0.012	1.2	100.2
2	1.0	1.03 ± 0.038	0.99 ± 0.027	2.7	99.2
3	10.0	10.46 ± 0.059	9.89 ± 0.45	4.5	98.9

[a] ELISA.

[b] Electrochemical sensor.

3.8. Selectivity, repeatability, and stability of the immunosensor

The selectivity of the fabricated biosensor was investigated by challenging other interfering agents at pH 7.0. Fig. 5A shows a sharp increase in the DPV response of 0.01 ng mL^{-1} PSA with an excess amount of non-target interfering substances (1 ng mL^{-1}), such as ascorbic acid, BSA, lysine, ovalbumin, glucose, lysozyme, sucrose, and lipase. The interferents used in our work are either the co-existed biomarkers or the analogues of the interferents. For example, ascorbic acid, glucose, lipase, or lysozyme exist in serum and were selected as the potential interferents. On the other hand, BSA was used as one of the interrerents, since it is analogous to human serum albumin (HSA, a primary component of serum protein). In addition, the current response of a mixture of PSA and other interferents also remarkably increased. This result indicated that the proposed biosensor had excellent selectivity. The PDV responses of five modified electrodes were investigated by detecting 0.01 ng mL^{-1} PSA to determine the repeatability of the biosensor. As shown in Fig. 5B, the five electrodes showed similar electrode responses in the presence of 0.01 ng mL^{-1} PSA and had a relative deviation (RSD) of 1.6%, which suggests excellent repeatability. For the stability of the sensor, the modified electrodes were stored at 4 °C for 14 d and then measured their DPV response. Here, the "stability" means the stability of DPV current of modified electrodes at the same storage conditions. As shown in Fig. 5C, the current responses of the constructed biosensors were over 95% of the primal response, showing the satisfactory stability.

3.9. Real sample analysis

Standard addition methods were used to detect PSA concentrations in artificial serum samples to evaluate the feasibility of the manufactured biosensor to analyze practical samples. Different concentrations of PSA (0.1, 1.0, and 10 ng mL^{-1}) were added to artificial serum samples, and their corresponding DPV measurements were recorded. The results were shown in Table 2. The sensor had recoveries from 98.9% to 100.2% with RSD values of 1.2%–4.5%, which suggest that the sensor had potential applications in PCa diagnosis and analysis. Furthermore, we also evaluated the feasibility of the constructed biosensor for PSA detection in prostate carcinoma cells and human sera. First, the PSA concentrations in the different prostate-related cells, including a normal prostatic epithelial cell (RWPE–1) and 2 prostate cancer cells with low PSA (DU145 and PC3) and high (LNCaP and 22RV1) expression, respectively. As shown in Fig. 6A, the PSA concentrations in the normal prostatic epithelial cell and low PSA–expressed prostate cancer cells were much lower than those in high PSA–expressed prostate cancer cells, which was consistent well with the result reported previously [50]. To verify the feasibility of the PSA determination of biosensor in real serum samples, the PSA concentrations in normal human and the PCa patients. The PSA concentration in the normal human serum were from 0.27 to 1.0 ng mL^{-1}. These values were lower than 4 ng mL^{-1}, which was considered the standard PSA concentration in the normal human sera according to the previous work [3]. However, in the case of PCa

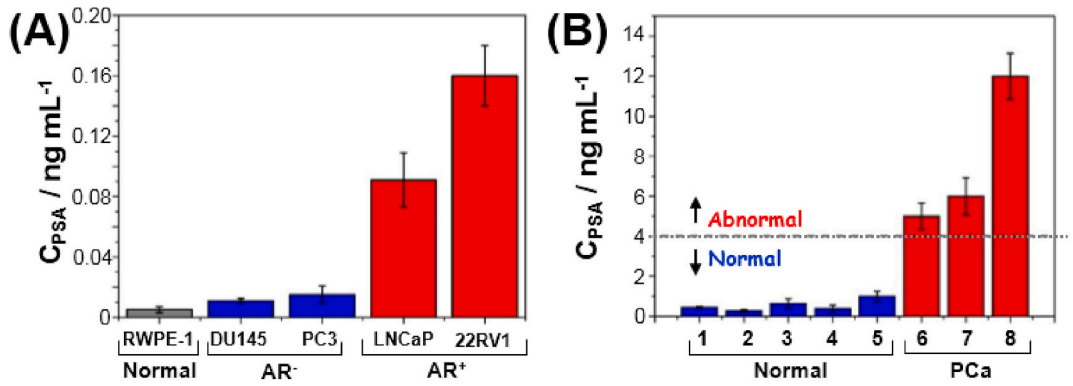

Fig. 6. PSA detection in different samples with proposed biosensor. PSA concentration of proteins extracted from five groups of different cells (**A**). AR^- and AR^+ indicated androgen receptor (AR) sensitive and AR insensitive prostate-related cells, which express less and more PSA, respectively. PSA concentration of serum samples from normal people and PCa patients (**B**). Error bar = standard deviation (SD), (n = 3).

patients, the PSA concentrations in sera were ranging from 5.0 to 12.0 ng mL^{-1} (Fig. 6B), which were much higher than those in normal sera. From these results, we concluded our biosensor could be successfully used to determine the PSA in different samples, including artificial serum, cell extract, or serum sample, providing a potential method for PSA determination in real samples.

4. Conclusions

A novel affinity peptide–antibody sandwich electrochemical biosensor based on PDA@BCN and AuPt@MnO_2@COF was developed in this study for the first time. The sensor showed a wider range of PSA concentrations with a low LOD. PDA@BCN as a sensing platform captured a large number of Ab1. The affinity peptide for PSA was bound to AuPt@MnO_2@COF as nanocarrier, and large amounts of redox-active MB probe were attached on the electrode surface. The sensor had high specificity, lower cost, excellent stability, and ideal repeatability in detecting PSA in practical samples. This design strategy has potential applications in detecting cancer biomarker for clinical diagnosis.

Credit author statement

Jing Zheng: Data curation, Investigation, Project administration, Validation, Writing – original draft. Hui Zhao: Conceptualization, Investigation, Supervision, Project administration, Validation, Writing – original draft. Conceptualization, Supervision, Validation. Guobao Ning: Data curation, Validation. Weijie Sun: Data curation, Validation. Li Wang: Conceptualization, Project administration. Huan Liang: Project administration, Conceptualization, Supervision, Validation. Hanbin Xu: Supervision, Validation. Chaoyong He: Data curation, Validation. Can-Peng Li: Conceptualization, Project administration, Supervision, Validation, Writing – review & editing, Funding acquisition.

Declaration of competing interest

The authors declare that they have no known competing financial interests or personal relationships that could have appeared to influence the work reported in this paper.

Acknowledgements

This work was financially supported by the Key Projects of Yunnan Natural Science Foundation (2018FA005), National Natural Science Foundation of China (21764005, 21565029), Key Research and Development Projects of Yunnan (2018BC005), Key Scientific and Technology Project of Yunnan (202002AE320005), Program for Excellent Young Talents of Yunnan University, and Program for Donglu Scholars of Yunnan University.

Appendix A. Supplementary data

Supplementary data to this article can be found online at https://doi.org/10.1016/j.talanta.2021.122520.

References

[1] J. Oto, Á.F. Pardo, M. Royo, D. Hervás, L. Martos, C.D.V. Donoso, M. Martínez, M. J. Heeb, F. España, P. Medina, S. Navarro, A predictive model for prostate cancer incorporating PSA molecular forms and age, Sci. Rep. 10 (2020) 2463, https://doi.org/10.1038/s41598-020-58836-4.

[2] L. Yang, H. Zhao, G. Deng, X. Ran, Y. Li, X. Xie, C. Li, Immunosensor for prostate-specific antigen using Au/Pd@flower-like SnO_2 as platform and Au@mesoporous carbon as signal amplification, RSC Adv. 5 (2015) 74046–74053, https://doi.org/10.1039/c5ra15046a.

[3] H. Liang, H. Xu, Y. Zhao, J. Zheng, H. Zhao, G. Li, C. Li, Ultrasensitive electrochemical sensor for prostate specific antigen detection with a phosphorene platform and magnetic covalent organic framework signal amplifier, Biosens. Bioelectron. 144 (2019) 111691, https://doi.org/10.1016/j.bios.2019.111691.

[4] J. Liu, B. Dong, W. Qu, J. Wang, Y. Xu, S. Y, X. Zhang, Using clinical parameters to predict prostate cancer and reduce the unnecessary biopsy among patients with PSA in the gray zone, Sci. Rep. 10 (2020) 5157, https://doi.org/10.1038/s41598-020-62015-w.

[5] D.S. Grubisha, R.J. Lipert, H. Park, J. Driskell, M.D. Porter, Femtomolar detection of prostate-specific antigen: an immunoassay based on surface-enhanced Raman scattering and immunogold labels, Anal. Chem. 75 (2003) 5936–5943, https://doi.org/10.1021/ac034356f.

[6] F. Yu, B. Persson, S. Löfas, W. Knoll, Surface plasmon fluorescence immunoassay of free prostate-specific antigen in human plasma at the femtomolar level, Anal. Chem. 76 (2004) 6765–6770.

[7] G. Ertürk, H. Özen, M. A. Tümer, B. Mattiasson, A. Denizli, Microcontact imprinting based surface plasmon resonance (SPR) biosensor for real-time and ultrasensitive detection of prostate specific antigen (PSA) from clinical samples, Sens. Actuators, B 224 (226) 823-832. https://doi.org/10.1016/j.snb.2015.10.093.

[8] K. Zhang, S. Lv, Z. Lin, D. Tang, CdS: Mn quantum dot-functionalized g-C_3N_4 nanohybrids as signal-generation tags for photoelectrochemical immunoassay of prostate specific antigen coupling DNAzyme concatamer with enzymatic biocatalytic precipitation, Biosens. Bioelectron. 95 (2017) 34–40, https://doi.org/10.1016/j.bios.2017.04.005.

[9] J. Liang, C. Yao, X. Li, Z. Wu, C. Huang, Q. Fu, C. Lan, D. Cao, Y. Tang, Silver nanoprism etching-based plasmonic ELISA for the high sensitive detection of prostate-specific antigen, Biosens. Bioelectron. 69 (2015) 128–134, https://doi.org/10.1016/j.bios.2015.02.026.

[10] S. Hu, S. Zhang, Z. Hu, Z. Xing, X. Zhang, Detection of multiple proteins on one dpot by laser ablation inductively coupled plasma mass spectrometry and application to immuno-microarray with element-tagged antibodies, Anal. Chem. 79 (2007) 923–929, https://doi.org/10.1021/ac061269p.

[11] J.P. Paraknowitsch, A. Thomas, Doping carbons beyond nitrogen: an overview of advanced heteroatom doped carbons with boron, sulphur and phosphorus for energy applications, Energy Environ. Sci. 6 (2013) 2839–2855, https://doi.org/10.1039/c3ee41444b.

[12] X. Li, P. Zhu, C. Liu, H. Pang, One step synthesis of boron-doped carbon nitride derived from 4-pyridylboronic acid as biosensing platforms for assessment of food safety, Chem. Commun. 55 (2019) 9160–9163, https://doi.org/10.1039/c9cc03787j.

[13] Y. Liu, K. Ai, L. Lu, Polydopamine and its derivative materials: synthesis and promising applications in energy, environmental, and biomedical fields, Chem. Rev. 114 (2014) 5057–5115, https://doi.org/10.1021/cr400407a.
[14] N. Wang, X. Zhao, H. Chen, L. Bai, H. Xu, W. Wang, H. Yang, D. Wei, L. Yang, Fabrication of novel electrochemical immunosensor by mussel-inspired chemistry and surface-initiated PET-ATRP for the simultaneous detection of CEA and AFP, React. Funct. Polym. 154 (2020) 104632, https://doi.org/10.1016/j.reactfunctpolym.2020.104632.
[15] X. Liu, D. Huang, C. Lai, G. Zeng, L. Qin, H. Wang, H. Yi, B. Li, S. Liu, M. Zhang, R. Deng, Y. Fu, L. Li, W. Xue, S. Chen, Recent advances in covalent organic frameworks (COFs) as a smart sensing material, Chem. Soc. Rev. 48 (2019) 5266–5302, https://doi.org/10.1039/c9cs00299e.
[16] Q. Zhang, H. Wei, L. Wang, J. Wang, L. Fan, H. Ding, J. Lei, X. Yu, B. Lu, Accessible COF-based functional materials for potassium-ion batteries and aluminum batteries, ACS Appl. Mater. Interfaces 11 (2019) 44352–44359, https://doi.org/10.1021/acsami.9b16280.
[17] B. Yao, J. Li, N. Huang, J. Kan, L. Qiao, L. Ding, F. Li, Y. Dong, Pd NP-loaded and covalently cross-Linked COF membrane microreactor for aqueous CBs dechlorination at room temperature, ACS Appl. Mater. Interfaces 10 (2018) 20448–20457, https://doi.org/10.1021/acsami.8b04022.
[18] P. Pachfule, A. Acharjya, J. Roeser, T. Langenhahn, M. Schwarze, R. Schomäcker, A. Thomas, J. Schmidt, Diacetylene functionalized covalent organic framework (COF) for photocatalytic hydrogen generation, J. Am. Chem. Soc. 140 (2018) 1423–1427, https://doi.org/10.1021/jacs.7b11255.
[19] X. Chen, Y. Li, L. Wang, Y. Xu, A. Nie, Q. Li, F. Wu, W. Sun, X. Zhang, R. Vajtai, P. M. Ajayan, L. Chen, Y. Wang, High-lithium-affinity chemically exfoliated 2D covalent organic frameworks, Adv. Mater. 31 (2019) 1901640, https://doi.org/10.1002/adma.201901640.
[20] V. Balakumar, J.W. Ryu, H. Kim, R. Manivannan, Y. Son, Ultrasonic synthesis of α-MnO_2 nanorods: an efficient catalytic conversion of refractory pollutant, methylene blue, Ultrason. Sonochem. 62 (2020) 104870, https://doi.org/10.1016/j.ultsonch.2019.104870.
[21] X. Zhou, L. Yang, X. Tan, G. Zhao, X. Xie, G. Du, A robust electrochemical immunosensor based on hydroxyl pillar[5]arene@AuNPs@g-C_3N_4 hybrid nanomaterial for ultrasensitive detection of prostate specific antigen, Biosens. Bioelectron. 112 (2018) 31–39, https://doi.org/10.1016/j.bios.2018.04.036.
[22] H.D. Jang, S.K. Kim, H. Chang, J. Choi, 3D label-free prostate specific antigen (PSA) immunosensor based on graphene–gold composites, Biosens. Bioelectron. 63 (2015) 546–551, https://doi.org/10.1016/j.bios.2014.08.008.
[23] B.P. Gray, K.C. Brown, Combinatorial peptide libraries: mining for cell-binding peptides, Chem. Rev. 114 (2014) 1020–1081, https://doi.org/10.1021/cr400166n.
[24] G.M. Gersuk, M.J. Corey, E. Corey, J.E. Stray, G.H. Kawasaki, R.L. Vessella, High-affinity peptide ligands to prostate-specific antigen identified by polysome selection, Biochem. Biophys. Res. Commun. 232 (1997) 578–582, https://doi.org/10.1006/bbrc.1997.6331.
[25] M. Hu, Y. Wang, J. Yang, Y. Sun, G. Xing, R. Deng, X. Hu, G. Zhang, Competitive electrochemical immunosensor for maduramicin detection by multiple signal amplification strategy via hemin@Fe-MIL-88NH2/AuPt, Biosens. Bioelectron. 142 (2019) 111554, https://doi.org/10.1016/j.bios.2019.111554.
[26] M. Zheng, T. Yuan, J. Shi, W. Cai, X. Wang, Photocatalytic oxygenation and deoxygenation transformations over BCN nanosheets, ACS Catal. 9 (2019) 8068–8072, https://doi.org/10.1021/acscatal.9b02550.
[27] J. Li, L. Cui, X. Zhang, Preparation and electrochemistry of one-dimensional nanostructured MnO_2/PPy composite for electrochemical capacitor, Appl. Surf. Sci. 256 (2010), https://doi.org/10.1016/j.apsusc.2010.02.028.
[28] X. Zhou, G. Zhao, M. Chen, W. Gao, X. Zhou, X. Xie, L. Yang, G. Du, Facile and green approach to prepare nanostructured Au@MnO_2 and its applications for catalysis and fluorescence sensing of glutathione in human blood, ACS Sustain. Chem. Eng. 6 (2018) 3948–3956. https://10.1021/acssuschemeng.7b04313.
[29] Y. Wu, L. Jiao, W. Xu, W. Gu, C. Zhu, D. Du, Y. Lin, Polydopamine-capped bimetallic AuPt Hydrogels enable robust biosensor for organophosphorus pesticide detection, Small 15 (2019) 1900632. https://10.1002/smll.201900632.
[30] V. Balakumar, J.W. Ryu, H. Kim, R. Manivannan, Y.A. Son, Ultrasonic synthesis of α-MnO_2 nanorods: an efficient catalytic conversion of refractory pollutant, methylene blue, Ultrason. Sonochem. 62 (2020) 104870, https://doi.org/10.1016/j.ultsonch.2019.104870.
[31] X. Zhou, X. Qian, X. Tan, X. Ran, Z. Li, Z. Huang, L. Yang, X. Xie, Water-soluble pillar[6]arene functionalized PdPt porous core-shell octahedral nanodendrites to construct highly sensitive and robust neuron-specific enolase immunosensor by host-guest chemistry assisted catalytic amplification, Anal. Chim. Acta 1068 (2019) 18–27, https://doi.org/10.1016/j.aca.2019.04.015.
[32] F. Li, Y. Li, J. Feng, Y. Dong, Y. Dong, P. Wang, L. Chen, Z. Chen, H. Liu, Q. Wei, Ultrasensitive amperometric immunosensor for PSA detection based on Cu_2O@CeO_2-Au nanocomposites as integrated triple signal amplification strategy, Biosens. Bioelectron. 87 (2017) 630–637, https://doi.org/10.1016/j.bios.2016.09.018.
[33] R. Wang, W. Liu, A. Wang, Y. Xue, L. Wu, J. Feng, A new label-free electrochemical immunosensor based on dendritic core-shell AuPd@Au nanocrystals for highly sensitive detection of prostate specific antigen, Biosens. Bioelectron. 99 (2018) 458–463, https://doi.org/10.1016/j.bios.2017.08.010.
[34] L. Li, J. Xu, X. Zheng, C. Ma, X. Song, S. Ge, J. Y, M. Yan, Growth of gold-manganese oxide nanostructures on a 3D origami device for glucose-oxidase label based electrochemical immunosensor, Biosens. Bioelectron. 61 (2014) 76–82, https://doi.org/10.1016/j.bios.2014.05.012.
[35] H. Wang, Y. Zhang, H. Yu, Dan Wu, H. Ma, Li He, B. Du, Q. Wei, Label-free electrochemical immunosensor for prostate-specific antigen based on silver hybridized mesoporous silica nanoparticles, Anal. Biochem. 434 (2013) 123–127, https://doi.org/10.1016/j.ab.2012.11.012.
[36] J. Feng, Y. Li, M. Li, F. Li, J. Han, Y. Dong, Z. Chen, P. Wang, H. Liu, Q. Wei, A novel sandwich-type electrochemical immunosensor for PSA detection based on PtCu bimetallic hybrid (2D/2D) rGO/g-C_3N_4, Biosens. Bioelectron. 91 (2017) 441–448, https://doi.org/10.1016/j.bios.2016.12.070.
[37] Y. Shi, A. Wang, P. Yuan, L. Zhang, X. Luo, J. Feng, Highly sensitive label-free amperometric immunoassay of prostate specific antigen using hollow dendritic AuPtAg alloyed nanocrystals, Biosens. Bioelectron. 111 (2018) 47–51, https://doi.org/10.1016/j.bios.2018.03.052.
[38] L. Suresh, P.K. Brahman, K.R. Reddy, J.S. Bondili, Development of an electrochemical immunosensor based on gold nanoparticles incorporated chitosan biopolymer nanocomposite film for the detection of prostate cancer using PSA as biomarker, Enzym. Microb. Technol. 112 (2018) 43–51, https://doi.org/10.1016/j.enzmictec.2017.10.009.
[39] L. Dai, Y. Li, Y. Wang, X. Luo, D. Wei, R. Feng, T. Yan, X. Ren, B. Du, Q. Wei, A prostate-specific antigen electrochemical immunosensor based on Pd NPs functionalized electroactive Co-MOF signal amplification strategy, Biosens. Bioelectron. 132 (2019) 97–104, https://doi.org/10.1016/j.bios.2019.02.055.
[40] R. Akter, M.A. Rahman, C.K. Rhee, Amplified electrochemical detection of cancer biomarker by enhanced precipitation using horseradish peroxidase attached on carbon nanotubes, Anal. Chem. 84 (2012) 6407–6415.
[41] Y. Chen, P. Yuan, A. Wang, X. Luo, Y. Xue, L. Zhang, J. Feng, A novel electrochemical immunosensor for highly sensitive detection of prostate-specific antigen using 3D open-structured PtCu nanoframes for signal amplification, Biosens. Bioelectron. 126 (2019) 187–192, https://doi.org/10.1016/j.bios.2018.10.057.
[42] V. Mani, B.V. Chikkaveeraiah, V. Patel, J.S. Gutkind, J.F. Rusling, Ultrasensitive immunosensor for cancer biomarker proteins using gold nanoparticle film electrodes and multienzyme-particle amplification, ACS Nano 3 (2009) 585–594, https://doi.org/10.1021/nn800863w.
[43] F. Farshchi, M. Hansazadeh, E. Solhi, Immunosensing of prostate cancer in human plasma samples using immobilization of antibody on the surface of mesoporous silica-modified silver nanoparticles and its immunocomplex with prostate-specific antigen, Anal. Methods. 11 (2019) 6159–6167, https://doi.org/10.1039/c9ay02058f.
[44] M. Srivastava, N.R. Nirala, S.K. Srivastava, R. Parkash, A comparative study of aptasensor *vs* immunosensor for label-free PSA cancer detection on GQDs-AuNRs modifed screen-printed electrodes, Sci. Rep. 8 (2018) 1923, https://doi.org/10.1038/s41598-018-19733-z.
[45] A.L. Jones, L. Dhanapala, T.A. Baldo, M. Sharafeldin, C.E. Krause, M. Shen, et al., Prostate cancer diagnosis in the clinic using an 8-protein biomarker panel, Anal. Chem. 2 (2021) 1059–1067, https://doi.org/10.1021/acs.analchem.0c04034.
[46] K. Kadimisetty, I.M. Mosa, S. Malla, J.E. Satterwhite-warden, T.M. Kuhns, R. C. Faria, N.H. Lee, J.F. Rusling, 3D-printed supercapacitor-powered electrochemiluminescent protein immunoarray, Biosens. Bioelectron. 77 (2016) 188–193, https://doi.org/10.1016/j.bios.2015.09.017.
[47] K. Kadimisetty, S. Malla, N.P. Sardesai, A.A. Joshi, R.C. Faria, N.H. Lee, J. F. Rusling, Automated multiplexed ECL immunoarrays for cancer biomarker proteins, Anal. Chem. 8 (2015) 4472–4478, https://doi.org/10.1021/acs.analchem.5b00421.
[48] Y. He, S. Xie, X. Yang, R. Yuan, Y. Cai, Electrochemical peptide biosensor based on in situ silver deposition for detection of prostate specific antigen, ACS Appl. Mater. Interfaces 24 (2015) 13360–13366, https://doi.org/10.1021/acsami.5b01827.
[49] Y. Wang, Y. Qu, G. Liu, X. Hou, Y. Huang, W. Wu, K. Wu, C. Li, Electrochemical immunoassay for the prostate specific antigen using a reduced graphene oxide functionalized with a high molecular-weight silk peptide, Microchim. Acta 182 (2015) 2061–2067, https://doi.org/10.1007/s00604-015-1552-2.
[50] H. Zhao, T. Ma, J. Lin, L. Liu, W. Sun, L. Guo, S. Wang, N.O. Otecko, Y. Zhang, Identifcation of valid reference genes for mRNA and microRNA normalisation in prostate cancer cell lines, Sci. Rep. 8 (2018) 1949, https://doi.org/10.1038/s41598-018-19458-z.